# Effects of geometry and tip speed ratio on the HAWT blade's root flow

**Buşra Akay[1], Daniel Micallef[2], Carlos J Simão Ferreira[1] and Gerard J W van Bussel[1]**

[1] Wind Energy Section, Faculty of Aerospace Engineering, Delft University of Technology, Kluyverweg 1, 2629HS Delft, The Netherlands.
[2] University of Malta, Faculty of Eng., Department of Mechanical Eng., Msida, MSD 2080 Malta.

E-mail: `b.akay@tudelft.nl`

**Abstract.** In this study, the effect of the parameters playing a role in the root flow behavior of HAWT are only partly understood. To better reveal the root flow properties, this study presents the progression of HAWT blade root flow at two different blade geometries and at two different tip speed ratios. The effects of the geometry and the tip speed ratio on the root flow behavior and on the evolution of the root flow features are investigated. This study aims to answer the following questions: (i) What are the effects of the blade geometry and tip speed ratio on the root flow behavior? (ii) How are the blade wake and the root vortex evolution affected by the change of these parameters? The analysis of the velocity fields shows that the radial flow behavior changes with different blade geometries but a remarkable difference in the radial flow behavior is not observed with the change of tip speed ratio. The formation of the wake is different at three test cases because of different loading that the blades are encountered. From the circulation distribution along the blades, while a strong root vortex can be observed in Blade 1, the bound vorticity along Blade 2 builds up gradually when moving outboard, and do not show a trace of a strong root vortex.

## 1. Introduction

The horizontal axis wind turbine (HAWT) wake has widely been investigated and reported in literature. A comprehensive review can be found in Vermeer et al. [1]. Among the near wake studies, the outboard region of the blade has taken the most of the attention; there has been limited research in the near wake of the root region. This may be because of two main reasons: (i) the power production from the root region is less significant important compared to the outboard region and (ii) the difficulties of both measurements and advanced calculations in the root region.

The root vortex has been studied numerically and experimentally (see Ebert and Wood [2], Whale et al. [3], Massouh and Dobrev [4], Ivanell et al. [5], Sherry et al. [6]). A more detailed literature review can be found in the previous study of the authors (see Akay et al. [7]). Ebert and Wood [8, 9, 2] analyzed the three velocity components and the formation of hub and tip vortices. The hub vortex analysis by Ebert and Wood [2] suggested that the hub vortices merging into a single hub vortex along the axis of rotation, opposing the experiments of Whale et al. [3], which showed the hub vortices merging with the tip vortex system. Whale et al. [3] were among

the first to show the usability of PIV in the wind turbine wake measurements. The vortex wake behind a HAWT rotor obtained from the experiments were analyzed and compared with the Rotor Vortex Lattice Method computations at different tip speed ratios. They also mentioned the existence of the inboard vorticity which was associated by flow blockage at the blade root section. In the experiments of Massouh and Dobrev [4], a small commercial wind turbine rotor was used for a PIV assessment of the wake. A large expanding inner vorticity was observed in their experiments and it was stated that the cause of the expanding hub vortex sheet was not related with the high solidity of the inboard region. In this study, it was inferred that the observed root vortex formation may be different at other rotor geometries.

The present research aims to understand the evolution of root flow features at different conditions such as different blade geometry and different tip speed ratios. For this purpose, stereoscopic particle image velocimetry (PIV) experiments were performed on two different HAWT blade models at different tip speed ratios. The three components of the velocity distributions in the blade root region at different azimuth angles along the wake region, at different radial locations in the chordwise direction, were measured in the experiments. The vorticity distributions were calculated by using the velocity distributions obtained from the experiments. In this study, three test cases are analyzed. In the following section, the experimental facility will be described including the wind tunnel, HAWT model, PIV apparatus and set-up. Following on this, the uncertainty of the PIV field is assessed.In the first part of the results and discussions, velocity and vorticity distribution in the near wake region are investigated. The analysis of velocity and vorticity in the chordwise direction are continued in the second part of the results and discussion with the calculation of circulation and the strength of the trailing voriticies. Finally, the key results of this research and the main conclusions are given.

## 2. Experiments
### 2.1. Wind tunnel and HAWT model
The experiments were performed at the Open Jet Facility (OJF) of the Aerospace Faculty of Delft University of Technology (TU Delft). The OJF is a closed circuit wind tunnel which has 2.85m diameter octagonal jet exit. This wind tunnel has a test section 6m x 6m x 11m (width x height x length). The inflow velocity in the test section can reach up to 35m/s and the turbulence intensity of the tunnel is relatively low, around 0.28%, which may vary depending on the operating speed.

The rotor model used in the experiment is a two-bladed horizontal axis wind turbine model with a 1m radius. In the experiments, two different blade geometries were used. The geometry of the blades are presented in Figure 2. A DU96-W-180 airfoil profile is used over the entire span of both blades except for the region connecting to the hub. The chord and twist distributions of the experimental blades along the span is represented in Figure 1. Since the local blade solidity (c/r) was shown to be the most relevant parameter for the corrections from 2D aerodynamic data [10], *Blade* 1 was designed with a relatively large c/r distribution at the maximum chord location to enhance the 3$D$ effects at the root region of the blade. *Blade* 2 was designed to have a clear root vortex with a large spanwise gradient of the maximum chord. However, in this design, stall delay is reduced to remove the secondary flow effects and to observe attached unsteady flow physics.

An essential component of the wind tunnel model is the "torque−axial" forces meter. This unit measures both the axial force and torque acting on the rotor shaft. In total, there are two force gauge units mounted in series (one after the other on the end of the rotor axis, space in the nose cone). Important to note that there is no interaction between the axial and radial loads. The measurement of these two components is carried out by means of strain gauges which are arranged on measuring springs. In this way, thrust and torque were measured. The

measurement conditions for each test and the forces during the measurements are summarized in Table 1.
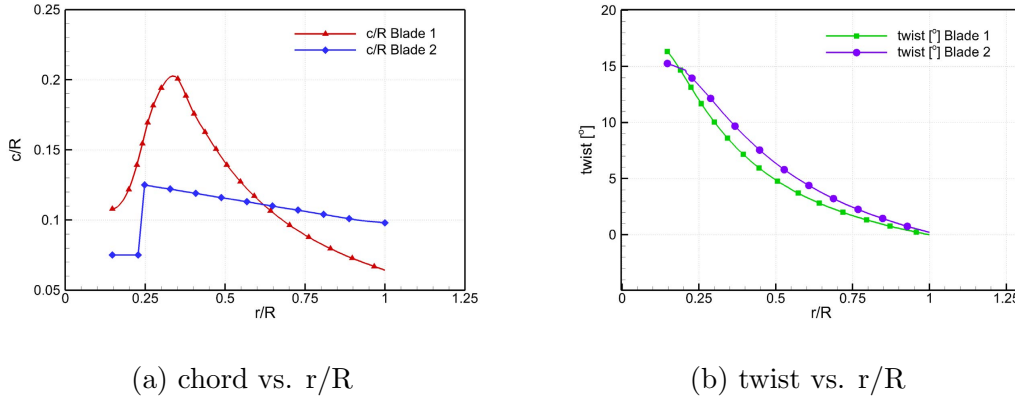


(a) chord vs. r/R                       (b) twist vs. r/R

Figure 1: Chord and twist distributions of the two model rotor blades.



(a) Blade 1                               (b) Blade 2
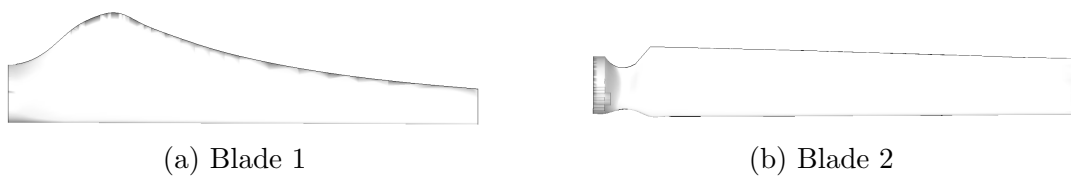
Figure 2: Planform representation of the blades.

Table 1: Measurement conditions.

| Test | Blade | yaw | $\lambda$ | $\omega$ [RPM] | $U_\infty$ [m/s] | $C_T$ | $C_P$ |
|------|-------|-----|-----------|----------------|------------------|-------|-------|
| 1 | Blade 1 | $0^o$ | 7 | 400 | 6 | 0.89 | 0.26 |
| 2 | Blade 2 | $0^o$ | 7 | 400 | 6 | 0.89 | 0.39 |
| 3 | Blade 2 | $0^o$ | 5 | 400 | 8.4 | 0.75 | 0.40 |

*2.2. PIV apparatus and set-up*

The flow was seeded with fog particles generated by a SAFEX Twin Fog generator using the SAFEX-Inside-Nebel fluid, a water soluble fog fluid, producing seeding particles with approximately 1 micron median diameter [11]. Seeding was given in the downstream of the measurement area. Hence, a homogenous mixture of the seeding in the flow was obtained in the test room. The field of view (FOV) was illuminated by double cavity pulsed Nd:YAG laser. The laser sheet had $\sim$ 3mm thickness at the FOV. Two 16 MPix cameras with 180mm lenses were used to lighten the field of view (FOV) at an aperture f♯ of 5.6 with tilt-lens Scheimpflug and Solidor adaptors at approximately 1.2 m, with a relative angle of about 40 deg. The cameras and the laser were fixed on a computerized traverse system so that they moved together. Therefore, it was not necessary to do calibrations at each FOV position. The synchronization between the laser pulses and the position of the rotating blade was achieved for the designed experiment with a triggering system in the hub. The PIV data were acquired with Davis 7.2 and evaluated with Davis 7.4 software.

Two different stereoscopic PIV setups were built to measure the three-components of velocity field in spanwise direction at different azimuth angles and in chordwise direction at different radial locations at the blade root region of HAWT model.

*Spanwise measurement set-up*

The spanwise measurement configuration is presented in Figure 3. Contrarily to the common PIV measurement procedure where the measurement plane is typically moved through a scanning device, in this study, the laser sheet is kept at the same location and the measurements are performed at different blade azimuth angles. The azimuth angle is assumed to be $\Theta = 0^o$ when the blade is at the 3 o'clock position when looking from upwind to downwind direction (see Figure 4) and rotation of the blade is positive in the clockwise direction. Measurements were performed from $\Theta = -45^o$ to $\Theta = 90^o$ azimuth angles at every $5^o$ on measurement planes with three components of velocity. Hence, the measurements at different azimuth angles allow constructing the entire 3D flow field, by assuming the flow is axisymmetric.

In order to investigate the full near wake of the rotor with sufficient resolution, the measurement area is divided into a number of field of views (FOVs), ensuring an overlap between every two FOVs. The cameras and the laser are fixed on a computerized traverse system so that they move together. Therefore, it is not necessary to repeat calibration at each FOV position. The synchronization between the laser pulses and the position of the rotating blade is achieved with a triggering system in the hub.
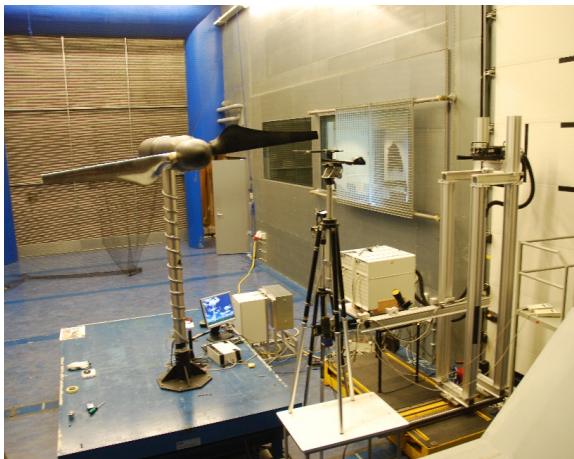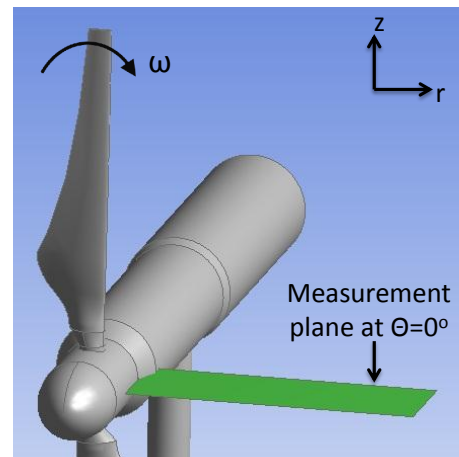


Figure 3: Spanwise measurement set-up in OJF.



Figure 4: Measurement plane location at $\Theta = 0^o$ (reference angle).

*Chordwise measurement set-up*

The chordwise measurement configuration is presented in Figure 5. In this set-up, contrarily to the spanwise measurement set-up, during the measurements the blade is kept at the same position but the laser sheet and the cameras are moved along the blade span. The measurements are performed when the blade is at $\Theta = 0^o$ azimuth angle, in other words where the blade is at the 3 o'clock position when looking from upwind to downwind direction (see Figure 4).

Chordwise measurements were performed at the suction and the pressure sides of the blade separately, due to the blade's shadow. After processing the two measurements separately, suction and pressure sides were "stitched" together. The measurements were performed at different radial locations in the root region of the blades.
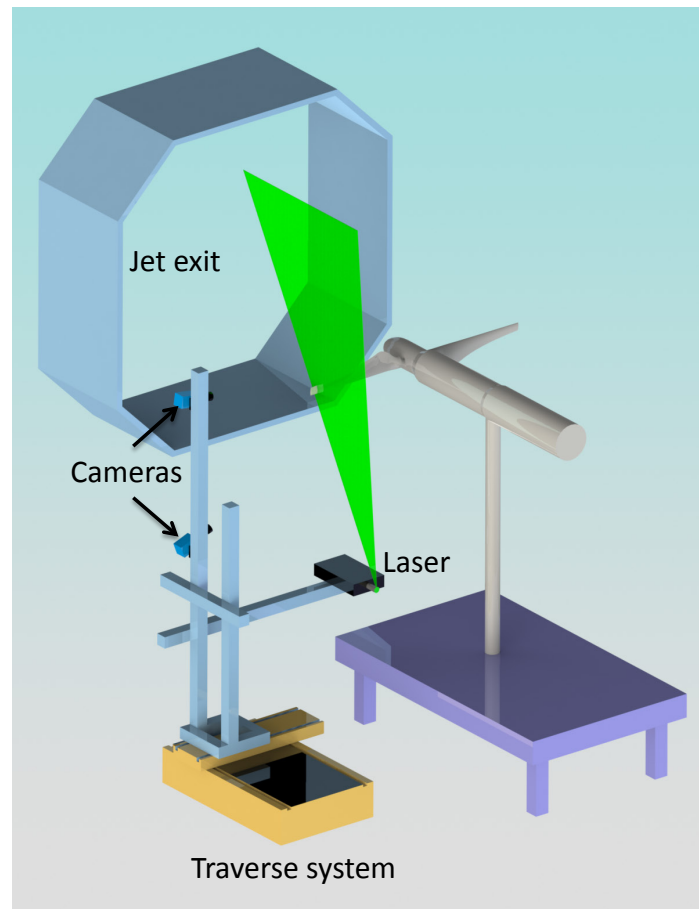
Figure 5: Schematic representation of the chordwise measurement set-up in the OJF.

## 3. Uncertainty of the PIV fields

The uncertainty on the velocity related quantities strongly depends on the uncertainty of the PIV measurements, and on the ensemble size. In a stereoscopic PIV setup, the cross-correlation uncertainty on the single velocity field is given by a contribution due to the registration error [12], and by the interrogation error [13]. While the registration error results from the misalignment of the calibration plane with the laser plane, the interrogation error results from the inaccuracy of the peak-detection in the cross-correlation procedure. Together with the cross-correlation uncertainty, the velocity fluctuations with respect to the mean are determined by both the phase unsteadiness of the timing systems and by the velocity fluctuations in the measurements. All these sources of uncertainties are considered random components which scale down with the $\sqrt{N}$, where $N$ is the number of velocity field acquired ($N = 100$ for this estimation). The velocity fluctuations, as evaluated from the root mean square in the acquired planes, depend upon the measurement location in the field. For this analysis Blade 2 $\lambda = 7$ data is used. The measured fluctuations in the averaged axial velocity ($\mu = \sqrt{\overline{u'u'}}$) field at a location in the upstream (r/R=0.87, x/R=-0.07) correspond to $\mu = 0.085 m/s$, which is the 1.42% of the incoming wind-tunnel free-stream velocity of $U_\infty = 6m/s$. The precision uncertainty due to fluctuations in the velocity field is defined as in Equation 1:

$$\varepsilon_\mu = \frac{\mu}{\sqrt{N}} Z_c \tag{1}$$

where $\mu$ represents the velocity root mean square, $\sqrt{U'^2}$, and $Z_c$ is 1.96 for a 95% confidence level [14]. The precision uncertainty at the same upstream position is calculated as $\varepsilon_{\mu,x} = 0.017$. At the same radial position but at around $x/R = 0.65$ in the wake region, the typical measured fluctuations in the planes in axial direction amount to $\mu_x = 0.082 \pm 0.016$ m/s. The fluctuations due to the jitter of the timing pixel correspond to $\varepsilon = \pm 0.02$ px in the raw images, or to $\pm 0.0174$ m/s at the tip.

The most relevant systematic sources of uncertainty in the present investigation are associated with the spatial resolution, and the peak-locking of the velocity fields. In the present investigation, it is rather difficult to estimate the error due to the finite spatial resolution, which depends on the measurement location and on the ratio between the size of the structures to be resolved and the window-size. Given the window-size used in the measurement technique, the minimum size of the structures ($\lambda_s/2$) that can be measured with an uncertainty corresponding to less than 10% is 2.75 mm [15]. The error due to peak-locking is quantified by statistical analysis on the histograms of the round-off values of velocities. Assuming a linear weight between a perfectly peak-locked distribution ($0.5px$ max error) and a Gaussian uniform one ($0pix$ error), the value corresponding to the measurement velocity histograms can be estimated. Therefore, the RMS of the maximum error due to peak-locking (PL) in the axial, radial and azimuthal directions are estimated to be 0.025 pix corresponding to 0.022 m/s, 0.048 pix corresponding to 0.043 m/s, and 0.03 pix corresponding to 0.027 m/s.

## 4. Results and Discussions

### 4.1. Velocity distributions in the near wake region

In this section, the phase-locked averaged velocities are presented in the blade near wake region, at different azimuth angles. The connections between the different FOVs are represented by dashed lines on the contour plots. In the present representations, the coordinate system used in the figures has a positive axial flow (free-stream direction) upward directed ($+x/R$), a positive radial flow moving from the blade root to the blade tip ($+r/R$), and a positive azimuthal flow represented by the out-of-plane direction. The velocity distributions presented here are non-dimensionalized by the free-stream velocity.

Having the distribution of the three components of velocity at and after the blade passage provides information about the flow evolution in the near wake region of the blade.

Figures 6, 7, and 8 present axial and azimuthal velocity distributions in the near wake region of the three test cases (Blade 1 at $\lambda = 7$, Blade 2 at $\lambda = 7$, Blade 2 at $\lambda = 5$) at $\Theta = 45^o$. From the comparison of axial and azimuthal velocity distributions of the three test cases, it can be seen that Blade 1 at $\lambda = 7$ has the lowest axial velocities in the near wake region and Blade 2 at $\lambda = 5$ has the highest velocities. In other words, Blade 1 at $\lambda = 7$ encounters the highest loads, Blade 2 at $\lambda = 5$ has the lowest loads.

The axial flow acceleration near the nacelle is observed in all three test cases. This maybe due to the vortical structures generated in the root region.

Positive azimuthal velocity areas show that the rotor wake region develops as expected with a rotation in the opposite direction of the blade rotation. Negative azimuthal velocities indicating areas, which are moving in the same direction with the blade rotation (into the paper), are also observed in the blade wake region of the three test cases. These regions are the manifestation of the presence of the viscous wake of the blades. The boundary layer material is shed from the blade and is subsequently conveyed in the downstream direction with the wake. The vortex wake is immersed into this viscous wake. It is noted that the thickness and the shape of the wake sheets (in axial direction) at three test cases differ from each other.

The axial movement of the wake sheets is best observed in the azimuthal velocity distribution of Blade 1 at $\lambda = 7$. It is about $r = 0.2$R for half a revolution and it becomes $\sim 0.4$R for a full revolution. In the second test case (Blade 2 at $\lambda = 7$), the axial translation of the wake sheets

is observed only for half a revolution and it is about $r = 0.4R$. This is consistent with the lower induction (higher axial velocities and lower loads) on the second blade test at the same $\lambda$.
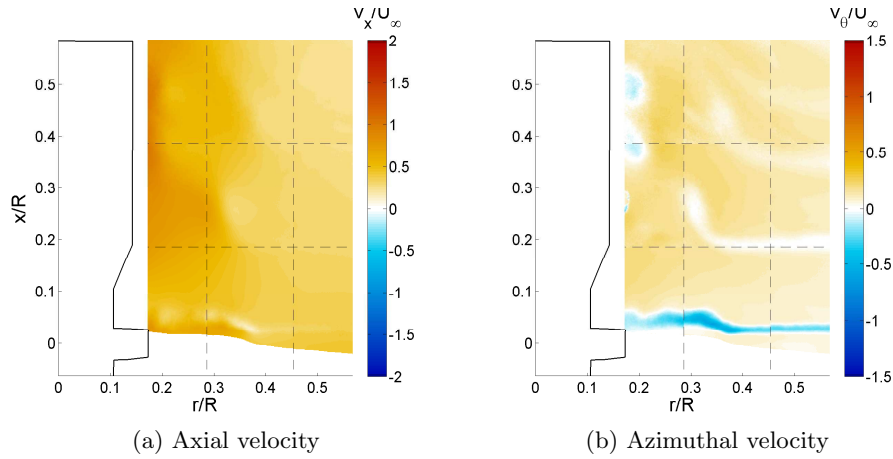


(a) Axial velocity                     (b) Azimuthal velocity

Figure 6: Blade 1 at $\lambda = 7$, dimensionless axial and azimuthal velocity distributions at $\Theta=45^o$ from stereoscopic PIV measurements. Inflow is in $+x/R$ direction.
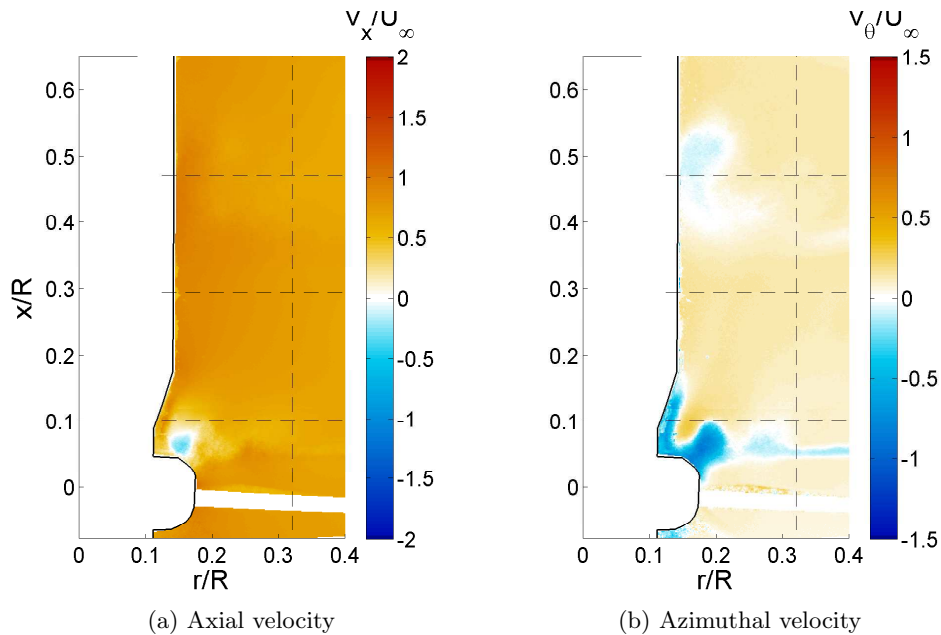

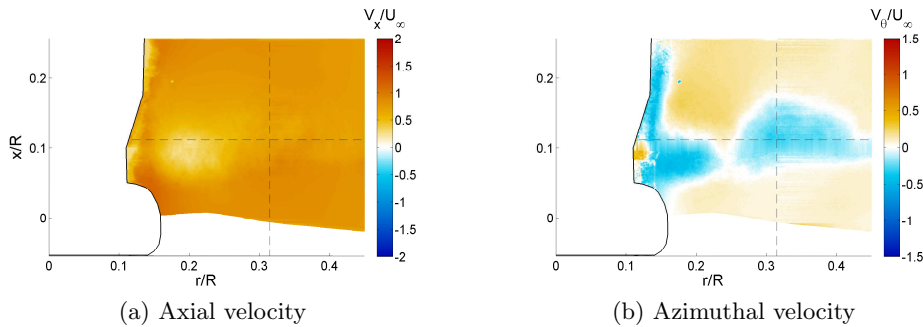
(a) Axial velocity                     (b) Azimuthal velocity

Figure 7: Blade 2 at $\lambda = 7$, dimensionless axial and azimuthal velocity distributions at $\Theta=45^o$ from stereoscopic PIV measurements. Inflow is in $+x/R$ direction.

Figures 9, 10, and 11 present radial velocity distributions in the near wake region of the blades at two blade azimuth angles for three test cases. While inboard radial flow is observed at around the maximum chord ($r/R \cong 0.3$) of Blade 1 in Figure 9-a, the flow is fully outboard in the wake region of Blade 2 at $\lambda = 7$ at $\Theta = 0^o$ (see Figure 10-a). For the same blade geometry (Blade 2) but at different $\lambda$, a small inboard flow motion is observed at around maximum chord ($r/R = 0.25$) (see Figure 11-a).

(a) Axial velocity                  (b) Azimuthal velocity

Figure 8: Blade 2 at $\lambda = 5$, dimensionless axial and azimuthal velocity distributions at $\Theta=45^o$ from stereoscopic PIV measurements. Inflow is in $+x/R$ direction.


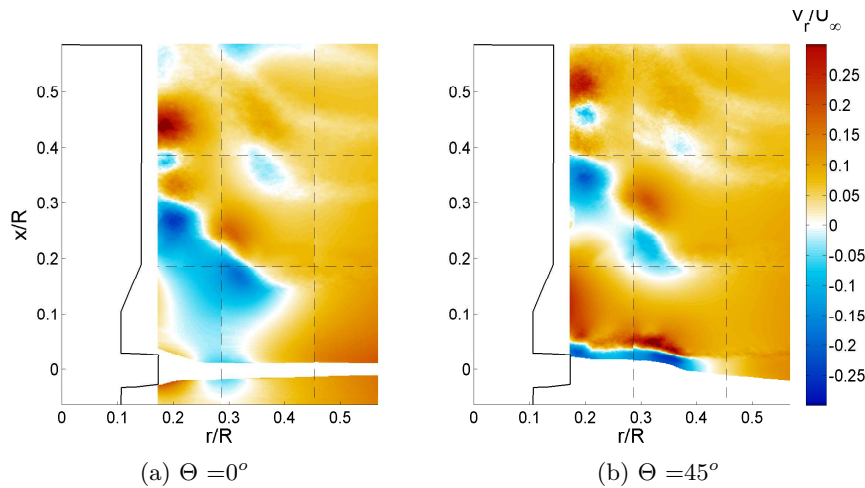
(a) $\Theta = 0^o$                  (b) $\Theta = 45^o$

Figure 9: Blade 1 at $\lambda = 7$, dimensionless radial velocity distribution from stereoscopic PIV measurements. Inflow is in $+x/R$ direction.

At $\Theta = 45^o$ azimuth angle, the boundary layer flow from the blade passage left in the wake region can be clearly seen with the inboard and outboard radial motion at three test cases. As expected the "scar" of the blade passage is observed further in the downstream for Blade 2 at $\lambda = 5$ than that for Blade 2 at $\lambda = 7$ due to higher freestream velocity. In radial velocity distributions for all three cases, the footprint of the vortical structures oriented in the azimuthal direction can also be observed just behind the blade and in the near wake region. The vortical structures just behind the blade coincide with the negative azimuthal velocities (wake sheets) noted in Figures 6-b, 7-b, 8-b.

Figures 12, 13 present the velocities extracted at $x/R = 0.05$ and $x/R = 0.1$ respectively from the velocity fields for three test cases. It is clearly seen that the velocities at $x/R = 0.05$ position are highly distorted by the presence of the blade. When radial velocities at $x/R = 0.1$ for three test cases are compared, it is noted that Blade 1 $\lambda = 7$ shows a different trend than Blade 2 cases. Blade 1 radial velocities show negative values around maximum chord position ($r/R \cong 0.3$). This demonstrates that the local geometry of the blade plays a role in the radial velocity distribution in close vicinity of the blade.

It can be observed from the comparison of the azimuthal velocities extracted at two downstream positions ($x/R = 0.05$ and $x/R = 0.1$) that there is a sudden azimuthal velocity increase in the root region when going inboard from around maximum chord position ($r/R \cong 0.3$)
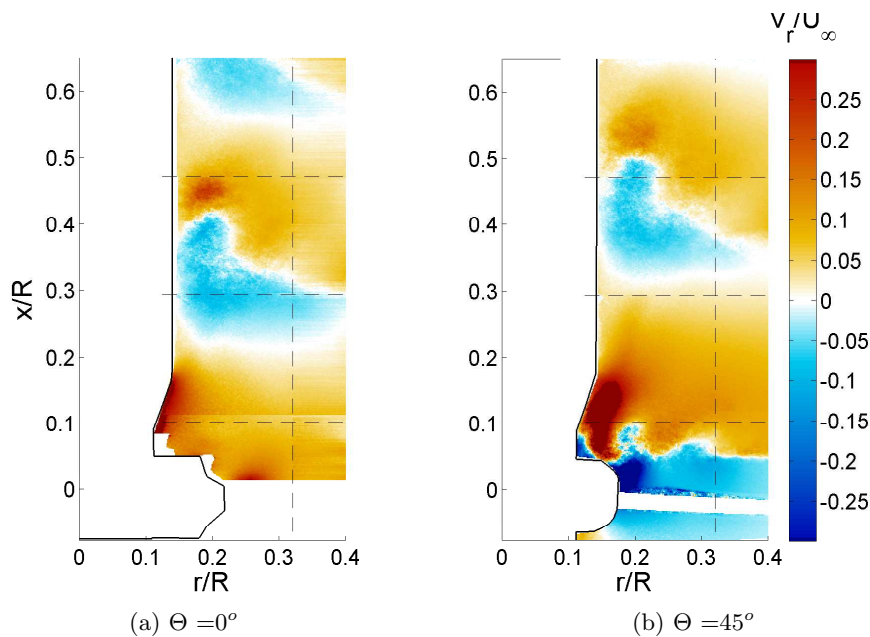
Figure 10: Blade 2 at $\lambda = 7$, dimensionless radial velocity distribution from stereoscopic PIV measurements. Inflow is in $+x/R$ direction.
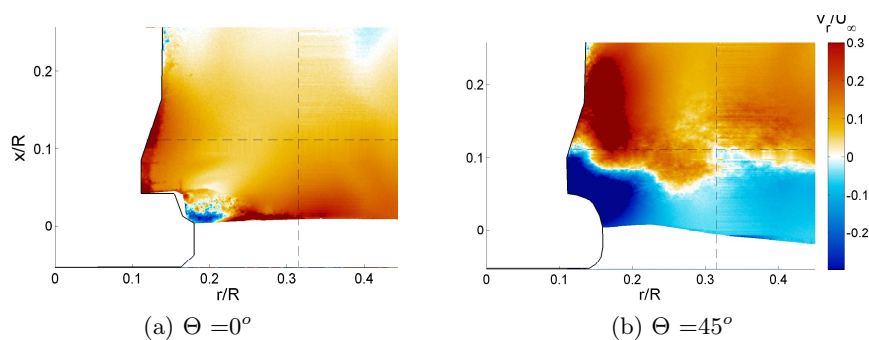


Figure 11: Blade 2 at $\lambda = 5$, dimensionless radial velocity distribution from stereoscopic PIV measurements. Inflow is in $+x/R$ direction.

towards nacelle (see Figure 12-b). On the other hand, a more constant velocity distributions are observed at $x/R = 0.1$. The differences in the azimuthal velocity distributions between the test cases originate from the both the differences in the geometries and also the differences in the flow separation from the blades.

### 4.2. Vorticity distributions in the near wake region
Azimuthal vorticity distributions are presented in Figures 14, 15 and 16 on 2D planes at two blade azimuth angles. It should be noted here that "vorticity creation" or "vorticity disappearance" may not be concluded by only analyzing the azimuthal vorticity distributions presented in this section. As it was already demonstrated and discussed in the previous study of the authors (see Akay et al. [7]), vorticity may change direction and can not only be observed in the azimuthal
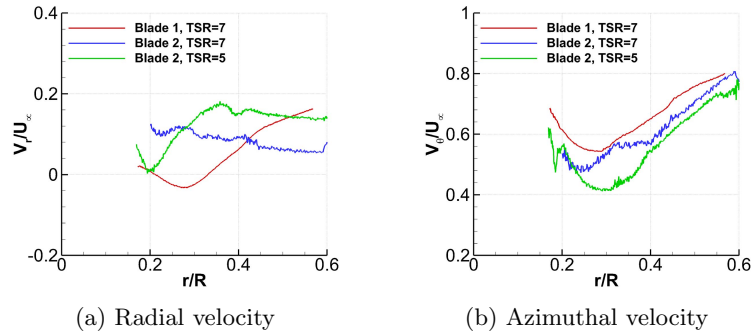
(a) Radial velocity          (b) Azimuthal velocity

Figure 12: Dimensionless velocity plots at $\Theta=0^o$, $x/R = 0.05$ for three test cases, from stereoscopic PIV measurements.



(a) Radial velocity          (b) Azimuthal velocity
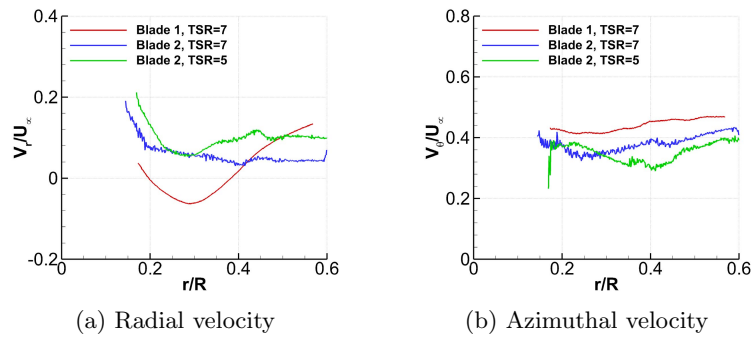
Figure 13: Dimensionless velocity plots at $\Theta=0^o$, $x/R = 0.1$ for three test cases, from stereoscopic PIV measurements.

direction.

The first point drawn from the comparison of vorticity distributions for Blade 1 and Blade 2 at $\lambda = 7$ is the number of vortices formed in the root region of the two blades. Two vorticity blobs are observed in Blade 1 case; one is emanated from the circular cross section of the blade (from $r/R \cong 0.15$ to $r/R \cong 0.2$) and the other one is around maximum chord position ($r/R \cong 0.3$). By contrast, only one vorticity blob is generated in Blade 2, emanated from the hub-blade connection part. In Blade 2, the vorticity is not as concentrated as in Blade 1. It is more diffused over a larger area.

Positive and negative vorticity just behind Blade 2 at $\Theta = 45^o$ is similar in behavior to what was discussed previously for Blade 1. For both blades, there is a vorticity sheet at $x/R \cong 0.05$ extending in radial direction. The comparison of Blade 1 and Blade 2 at $\lambda = 7$ shows that the evolution of the root vortex highly depends on the blade geometry and resulting circulation distribution.

From the comparison of vorticity distribution for Blade 2 at different $\lambda$ and at $\Theta = 45^o$, it can be noted that in Blade 2 $\lambda = 5$ at around $x/R = 0.08$ and $r/R = 0.17$ there is a more concentrated vortex blob. However, the vorticity in the leeward side of the blade is distributed in a larger area with positive and negative values. Again there is a vorticity sheet attached to the vortex blob extending outboard.

### 4.3. Spanwise bound vorticity and the strength of trailing vortex

It is possible to deduce the variation of the circulation along the blade radius by evaluating the velocity measurements at several spanwise positions of the blade. The circulation is calculated

(a) $\Theta = 0^o$
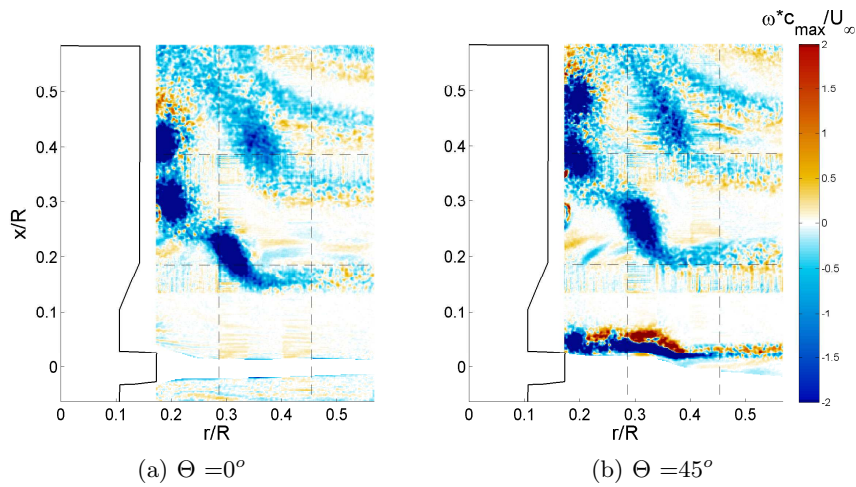
(b) $\Theta = 45^o$

Figure 14: Blade 1 at $\lambda = 7$, dimensionless azimuthal vorticity distributions calculated from stereoscopic PIV measurements. Inflow is in $+x/R$ direction.
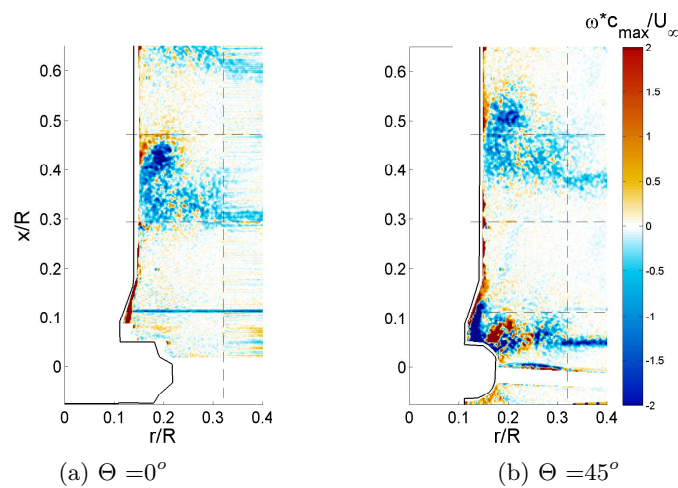


(a) $\Theta = 0^o$

(b) $\Theta = 45^o$

Figure 15: Blade 2 at $\lambda = 7$, dimensionless azimuthal vorticity distributions calculated from stereoscopic PIV measurements. Inflow is in $+x/R$ direction.
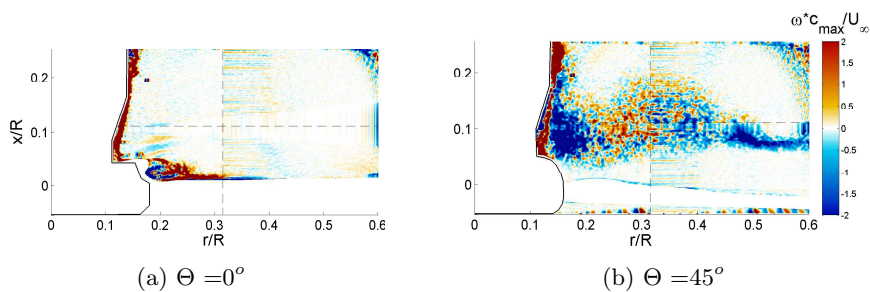


(a) $\Theta = 0^o$

(b) $\Theta = 45^o$

Figure 16: Blade 2 at $\lambda = 5$, dimensionless azimuthal vorticity distributions calculated from stereoscopic PIV measurements. Inflow is in $+x/R$ direction.

by integrating the velocities around a rectangular contour (see Figure 17) and it is defined by Equation 2.

$$\Gamma = \oint_C V.ds \tag{2}$$

where $V$ is the in plane velocity and $ds$ is the incremental length along the contour line. The calculations are performed for four different contour lengths and it is seen that there is no significant effect of contour length on the calculation of circulation from the PIV velocity data used in this analysis. Also, the strength of each trailing vortex is calculated from the change in circulation along the blade span.
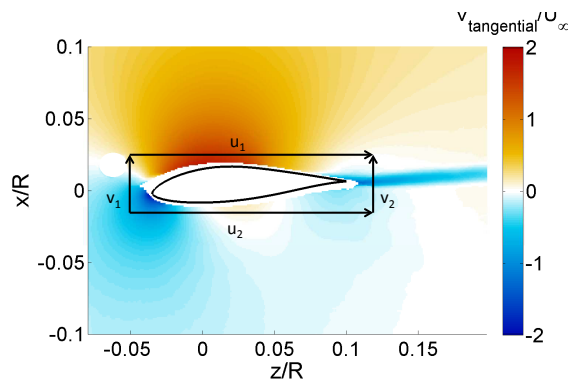


Figure 17: Representation of rectangular contour approach for circulation calculation. Non-dimensional tangential velocity contour at r/R=0.52.
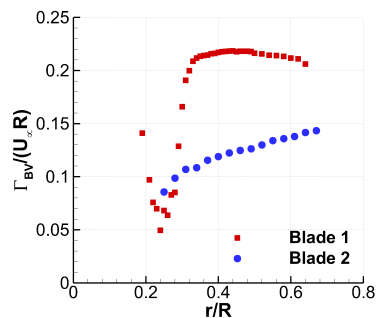


Figure 18: Blade 1 and Blade 2 at $\lambda = 7$, dimensionless spanwise bound vorticity obtained from the chordwise stereoscopic PIV experiments.
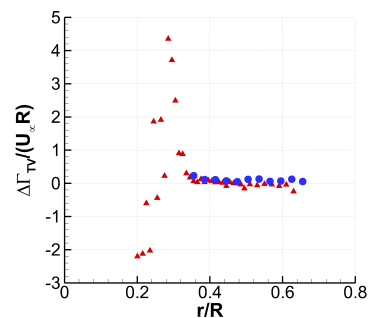
Figure 19: Dimensionless strength of trailing vortex derived from the bound circulation.

Figure 18 presents the dimensionless spanwise bound vorticity at several radial locations for Blade 1 and Blade 2 at $\lambda = 7$. While the mid-board region shows an almost constant circulation distribution at Blade 1, Blade 2 has lower values but a slightly increasing trend in this region. The sudden drop in the circulation at the root region of Blade 1 shows the position of the root vortex formed at around $c_{max}$ ($r/R \cong 0.3$). The strength of the each trailing vortices is derived from the change in circulation and is presented in Figure 19. In Blade 1, a strong root vortex

is observed with the higher strength values in the root region. While for Blade 1, the strength of the trailing vortices in the mid-board region is very close to zero, Blade 2 has higher values in this region. It can be noted in the circulation distribution of Blade 2 that trace of a strong root vortex is missing and the bound vorticity is gradually built up when moving outboard (see Figure 18). This can also be seen with a constant trailing vorticity distribution in Figure 19.

## 5. Conclusion

In this study, the evolution of HAWT blade root flow for different blade geometries and at different tip speed ratios were analyzed. For this purpose, stereoscopic PIV experiment performed on a HAWT model in an open-jet wind tunnel. The velocity and vorticity fields in the near wake region at different blade azimuth angles for three test cases were analyzed. Furthermore, the bound vorticity and the strength of the trailing vorticity were compared for Blade 1 and Blade 2 at $\lambda = 7$.

This study shows that the radial flow behavior changes with different blade geometries but a remarkable difference in the radial flow behavior is not observed with the change of tip speed ratio.

Moreover, wake vorticity sheets are clearly observed in the azimuthal velocity distributions with negative values in all the test cases. However, the formation of the wake is different at three test cases because of different loading that the blades are encountered.

An increase in the axial velocity just behind the blade in the region very close to the nacelle is observed at three test cases. While the velocity increase may be explained with the presence of the vortices in the root region, it might also be caused by the lack of aerodynamic thrust in this part of the rotor disc. This will lead to an increase of axial velocities.

Furthermore, circulation distribution of Blade 1 at $\lambda = 7$ shows a strong root vortex with a sudden drop at the maximum chord ($r/R \cong 0.3$). And the comparison of the circulation distributions of two blades shows that Blade 1 is a blade designed to perform according to optimal loading. Trace of a strong root vortex is not observed in the circulation distribution of Blade 2 at $\lambda = 7$ and the bound vorticity builds up gradually when moving outboard. This study demonstrates that the evolution/strength of the root vortex highly depends on the blade geometry and the distribution of circulation.

## References

[1] L. Vermeer, J. Sørensen, and A. Crespo, "Wind turbine wake aerodynamics," *Progress in Aerospace Sciences*, vol. 39, pp. 467–510, 2003.

[2] P. Ebert and D. Wood, "The near wake of a model horizontal-axis wind turbine, Part 3: Properties of the tip and hub vortices," *Renewable Energy*, vol. 22, pp. 461–472, 2001.

[3] J. Whale, C. Anderson, R. Bareiss, and S. Wagner, "An experimental and numerical study of the vortex structure in the wake of a wind turbine," *Journal of Wind Engineering and Industrial Aerodynamics*, vol. 84, pp. 1–21, 2000.

[4] F. Massouh and I. Dobrev, "Exploration of the vortex wake behind of wind turbine rotor," *Journal of Physics: Conference Series 012036*, vol. 75, 2007.

[5] S. Ivanell, J. N. Sørensen, R. Mikkelsen, and D. Henningson, "Numerical analysis of the tip and root vortex position in the wake of a wind turbine," *Journal of Physics: Conference Series 012035*, vol. 75, 2007.

[6] M. Sherry, J. Sheridan, and D. L. Jacono, "Horizontal axis wind turbine tip and root vortex measurements," in *15th Int Symp on Applications of Laser Techniques to Fluid Mechanics*, 2010.

[7] B. Akay, D. Ragni, C. Ferreira, and G. van Bussel, "Experimental investigation of the root flow in a horizontal axis wind turbine," *Wind Energy*, vol. DOI: 10.1002/we.1620, 2013.

[8] P. Ebert and D. Wood, "The near wake of a model horizontal-axis wind turbine-I: Experimental arrangements and initial results," *Renewable Energy*, vol. 12, pp. 225–243, 1997.

[9]  P. Ebert and D. Wood, "The near wake of a model horizontal-axis wind turbine-II: General features of the three-dimensional flowfield," *Renewable Energy*, vol. 18, pp. 513–534, 1999.

[10] H. Snel, R. Houwink, G. van Bussel, and A. Bruining, "Sectional prediction of 3D effects for stalled flow on rotating blades and comparison with measurements," in *1993 European Community Wind Energy Conference Proceedings, Lubeck-Travemunde, Germany*, 1993.

[11] *Nebelfluid Partikelgrosse, 7.5 Droplet size distribution.*

[12] A. Prasad and R. Adrian, "Stereoscopic particle image velocimetry applied to liquid flows," *Exp Fluids*, vol. 15, pp. 49–60, 1993.

[13] J. Westerweel, D. Dabiri, and M. Gharib, "The effect of a discrete window offset on the accuracy of cross-correlation analysis of digital PIV recordings," *Experiments in Fluids*, vol. 23, pp. 20–28, 1997.

[14] H. Bruun, *Hot-Wire Anemometry: Principles and signal analysis*. Oxford University Press, 1995.

[15] F. Schrijer and F. Scarano, "Effect of predictor-corrector filtering on the stability and spatial resolution of iterative PIV interrogation," *Exp Fluids*, vol. 45, pp. 927–941, 2008.